Open access • Posted Content • DOI:10.1101/2020.10.26.356063

A toolbox for imaging RIPK1, RIPK3 and MLKL in mouse and human cells

Andre L. Samson, Andre L. Samson, Cheree Fitzgibbon, Komal Patel ...+19 more authors

Institutions: University of Melbourne, Walter and Eliza Hall Institute of Medical Research

Published on: 26 Oct 2020 - bioRxiv (Cold Spring Harbor Laboratory)

Topics: Necroptosis and RIPK1

A toolbox for imaging RIPK1, RIPK3 and MLKL in mouse and human cells

André L. Samson[1,2*], Cheree Fitzgibbon[1], Komal M. Patel[1], Joanne M. Hildebrand[1,2], Lachlan W. Whitehead[1,2], Joel S. Rimes[1,2], Annette V. Jacobsen[1,2], Christopher R. Horne[1,2], Xavier J. Gavin[1,2], Samuel N. Young[1], Kelly L. Rogers[1,2], Edwin D. Hawkins[1,2], James M. Murphy[1,2*]

[1]Walter and Eliza Hall Institute of Medical Research, 1G Royal Parade, Parkville, VIC 3052, Australia

[2]Department of Medical Biology, University of Melbourne, Parkville 3052, Australia

[*]Please address correspondence to samson.a@wehi.edu.au (ALS) or jamesm@wehi.edu.au (JMM)

Running title: Imaging necroptosis in mouse and human cells

Keywords: kinase, pseudokinase, cell death, programmed necrosis, fixative

ABSTRACT

Necroptosis is a lytic, inflammatory cell death pathway that is dysregulated in many human pathologies. The pathway is executed by a core machinery comprising the RIPK1 and RIPK3 kinases, which assemble into necrosomes in the cytoplasm, and the terminal effector pseudokinase, MLKL. RIPK3-mediated phosphorylation of MLKL induces oligomerization and translocation to the plasma membrane where MLKL accumulates as hotspots and perturbs the lipid bilayer to cause death. The precise choreography of events in the pathway, where they occur within cells, and pathway differences between species, are of immense interest. However, they have been poorly characterized due to a dearth of validated antibodies for microscopy studies. Here, we describe a toolbox of antibodies for immunofluorescent detection of the core necroptosis effectors, RIPK1, RIPK3 and MLKL, and their phosphorylated forms, in human and mouse cells. By comparing reactivity with endogenous proteins in wild-type cells and knockout controls in basal and necroptosis-inducing conditions, we characterise the specificity of frequently-used commercial and recently-developed antibodies for detection of necroptosis signaling events. Importantly, our findings demonstrate that not all frequently-used antibodies are suitable for monitoring necroptosis by immunofluorescence microscopy, and methanol- is preferable to paraformaldehyde-fixation for robust detection of specific RIPK1, RIPK3 and MLKL signals.

INTRODUCTION

Cell death by necroptosis is thought to have originated as an ancestral host defence mechanism, which is reflected in the breadth of pathogen-encoded proteins that inhibit the pathway[1, 2, 3, 4, 5, 6]. In addition to reported innate immunity functions[7, 8, 9], the dysregulation of necroptosis has been implicated in a range of pathologies, including ischemic-reperfusion injuries, such as in the kidney[10, 11] and heart[12], and inflammatory diseases[13, 14, 15, 16], including inflammatory bowel disease[17]. Accordingly, there is widespread interest in therapeutically-targeting the pathway to counter human disease. Owing to the recent identification of the terminal effectors of the pathway, RIPK3 (in 2009)[1, 18, 19] and MLKL (in 2012)[20, 21], however, the extent of indications attributable to necroptotic cell death is poorly understood. Precisely defining pathologies impacted by necroptosis has posed a challenge owing to the dearth of antibodies validated to specifically detect members of the pathway and their activated (phosphorylated) forms in fixed cells and tissues. As a result, the contribution of necroptosis to many pathologies remains a subject of ongoing debate[22, 23, 24, 25].

Necroptotic cell death signaling is initiated by ligation of death receptors, such as the TNF receptor 1, or pathogen detectors, such as Toll-like receptors 3 and 4 and the ZBP1/DAI intracellular viral RNA sensor protein. In cellular contexts where the activities of the Inhibitors of Apoptosis proteins (IAPs) E3 Ubiquitin ligase family and the proteolytic apoptotic effector, Caspase-8, are depleted or compromised, necroptosis ensues. The precise choreography of necroptotic signaling is still emerging, although recent studies have defined key events and checkpoints in the pathway[26, 27, 28, 29]. Following pathway induction, RIPK1 autophosphorylation prompts hetero-oligomerization with RIPK3 via an amyloid-forming motif in the region C-terminal to their kinase domains termed the RHIM (RIP Homotypic Interaction Motif) to form a cytoplasmic platform known as the necrosome[30, 31, 32]. Upon RIPK3 activation by autophosphorylation within necrosomes[33, 34], RIPK3 is primed to phosphorylate the activation loop of the MLKL pseudokinase domain to activate MLKL's killing function[14, 20, 27, 28, 35, 36, 37, 38, 39]. In the case of human MLKL, dormant MLKL appears to be at least in

part pre-associated with RIPK3 in the cytoplasm[20, 40], and stable recruitment to necrosomes appears to be an essential checkpoint in MLKL activation[28]. In the case of mouse MLKL, a transient interaction between RIPK3 and MLKL appears to be sufficient for MLKL activation in mouse cells[35, 36, 37]. Regardless of species, MLKL phosphorylation is thought to provoke a conformational change in the pseudokinase domain that leads to oligomerization and unmasking of the killer N-terminal four-helix bundle (4HB) domain[37, 40, 41, 42, 43]. The human MLKL 4HB domain likely engages chaperones to facilitate translocation to the plasma membrane via an actin-, Golgi- and microtubule-dependent mechanism, where MLKL accumulates in hotpots. When a threshold is surpassed, the 4HB domains of MLKL permeabilize the membrane to induce cell death[26, 29].

While biochemical studies have defined these steps and checkpoints, visualizing the spatiotemporal dynamics of endogenous proteins during in necroptosis using microscopy-based approaches has proven challenging in the absence of antibodies that have been validated for target specificity. Similarly, the lack of validated reagents poses a challenge to immunohistochemical staining of patient tissue sections, and therefore attribution of a role for necroptosis in pathologies, because knockout tissue controls are not available. Here, we have established procedures for staining endogenous RIPK1, RIPK3 and MLKL, and their phosphorylated forms, in fixed mouse and human cells. While several frequently-used antibodies were found to be suitable for selectively staining these proteins, as validated by comparisons with cells deficient for each protein, many exhibited non-specific staining and are therefore unsuitable for immunofluorescence and immunohistochemistry. Our studies also highlight the importance of validating antibody compatibility with fixation methods. In most cases, paraformaldehyde fixation ablated epitopes, presumably because RIPK3 and MLKL are lysine-rich and prone to modification by crosslinking, whereas methanol fixation enabled specific detection of these proteins. Due to the sequence divergence between mouse and human RIPK3 and MLKL[41, 43, 44, 45, 46], it was not possible to specifically-detect proteins across species using a single reagent, which necessitated the development of a new antibody that specifically detected mouse

MLKL. Collectively, our studies present a toolbox of selective antibodies that will enable critical analysis of the chronology, checkpoints and kinetics of necroptotic signaling in mouse and human cells.

RESULTS

Immunofluorescent detection of human MLKL

We recently described a monoclonal antibody, clone 10C2 (source: WEHI Antibody Facility, in-house), that recognises an epitope centred on residues 413-471 of human MLKL[29] (Fig. 1a). The initial screen that identified this clone suggested it yielded specific immunosignals when cells were fixed with methanol, but not when cells were fixed with paraformaldehyde. Organic solvents such as methanol preserve cells by precipitating proteins, whereas aldehyde-based agents such as paraformaldehyde fix cells by crosslinking lysines and other primary amines. Because human MLKL is lysine-rich (93rd percentile in the cytoplasmic and membrane-associated proteome), paraformaldehyde likely causes widespread crosslinking of MLKL, which in turn masks epitopes and reduces immunoreactivity. As several other necroptotic proteins are lysine-rich, we considered whether the choice of fixative was a critical variable for robust immunodetection of MLKL, RIPK3 and RIPK1 in human and mouse cells. Accordingly, we compared the performance of 22 antibodies for immunofluorescent staining of human HT29 cells and mouse dermal fibroblasts (MDFs) - two cellular models that are well-characterized to undergo necroptosis when treated with TNF, Smac-mimetic and IDN-6556 (herein referred to as TSI)[5, 28, 29, 44, 47]. To quantitatively gauge the performance of each antibody, their immunosignals were characterized in four ways: 1) A ratio of the immunofluorescent signals between a positive and negative control. This produces a signal-to-noise curve that estimates 'specific signal abundance' (Fig. 1b). For testing phospho-specific antibodies, wild-type cells undergoing necroptosis were used as a positive control and untreated wild-type cells as a negative control (Fig. S1). For testing all other antibodies, untreated wild-type cells

were used as a positive control and relevant knockout cells as a negative control. 2) Micrographs were gated so that the minimum/maximum immunosignals corresponded to the 5th/95th percentiles of the signal-to-noise curve (Fig. 1b). 3) The percentage of total signals that fall within this gate were determined to show how much signal from the positive control was considered specific (Fig. 1c). 4) Antibodies were immunoblotted against positive and negative controls to independently assess their specificity.

Using this approach, we confirmed that clone 10C2 specifically detects endogenous human MLKL in methanol-fixed, but not paraformaldehyde-fixed cells (Fig. 1d-f). The 10C2 clone produces a favourable immunostaining profile, where the specific signals are abundant (Fig. 1e) and these specific signals represent the majority of all detectable signals (Fig.1d). We recently developed another MLKL-specific antibody, clone 7G2 (source: in-house), that recognises an epitope centred on αF-αG loop the C-lobe of the human MLKL pseudokinase domain, which differs to the site recognised by the 10C2 clone[29]. Despite binding a distinct site in human MLKL to 10C2, the 7G2 clone shows similar specificity for human MLKL in immunoblot analyses and only yields specific immunofluorescent signals on methanol-fixed cells (Fig. 1d-f). Notably, clone 7G2 is inferior to clone 10C2 for immunofluorescence studies, because specific signals were less abundant (Fig. 1e) and were a minor fraction of all detectable signals (Fig.1d).

We observed that clone EPR9514 (source: Abcam), an antibody raised against phospho-S358 of human MLKL[48], which is a hallmark of MLKL activation during necroptosis[20], produced specific and comparable immunofluorescent signals in both methanol- and paraformaldehyde-fixed cells undergoing necroptosis (Fig. 1e). As MLKL can be disulfide-crosslinked during necroptosis[49, 50] (Fig. S2A-B), we tested whether fixation in the presence of *N*-ethylmaleimide (NEM) to prevent further disulfide bonding, or post-fixative treatment with Tris(2-carboxyethyl)phosphine (TCEP) to reduce disulfide bonds, altered the immunofluorescent detection of phospho-MLKL by clone EPR9514. However, neither preventing nor reducing disulfide bonds in fixed cells precluded the

immunodetection of MLKL by clone EPR9514 (Fig. S2C-D). Indeed, disulfide-crosslinking may be a by-product of MLKL activation given that recombinant human MLKL oligomerizes in the absence of disulfide bonds (Fig. S2E).

Two other anti-human MLKL antibodies were found to be non-specific (Novus Biological clone 954702; and Sigma-Aldrich M6697, a polyclonal antibody raised against residues 58-70; Fig. 1a and 1e), with equivalent signal intensity and diffuse staining observed in wild-type and *MLKL*$^{-/-}$ cells. Lastly, immunoblotting confirmed that clones 10C2, 7G2 (both in-house) and EPR9514 (Abcam) were highly-specific with bands corresponding to human MLKL's molecular weight of 54kDa observed in wild-type but not *MLKL*$^{-/-}$ HT29 cell lysates. In contrast, clone 954702 (Novus Biological MAB9187) and the Sigma-Aldrich M6697 polyclonal antibody were non-specific, with multiple bands not corresponding to the molecular weight of MLKL observed in both wild-type and *MLKL*$^{-/-}$ HT29 cell lysates (Fig. 1g).

In summary, three of the five antibodies that were tested selectively recognised human MLKL in methanol-fixed cells (clones 10C2, 7G2 and EPR9514) and, accordingly, we recommend methanol fixation for detecting endogenous human MLKL by immunofluorescence. Under these conditions, cytoplasmic forms of MLKL could be detected using the 10C2 and 7G2 clones, and phospho-MLKL accumulating at the cell periphery with the EPR9514 clone (Fig. 1f). These data underscore the importance of careful consideration of fixation method when using MLKL as a histological marker of necroptosis.

Immunofluorescent detection of human RIPK3

We next assessed five anti-human RIPK3 antibodies (Fig. 2a). Two antibodies raised against the C-terminus (source: ProSci 2283, Novus Biological NBP2-24588) and one antibody raised against the N-terminus of RIPK3 (source: Novus Biological MAB7604, clone 780115) yielded non-specific signals via both immunofluorescence and immunoblotting (Fig. 2b-e). Our recently described

158 antibody, clone 1H2 (source: in-house)[5], detected RIPK3 via immunofluorescence in methanol-fixed,
159 but not paraformaldehyde-fixed cells. However, most of the immunofluorescent signals produced by
160 1H2 were non-specific (Fig. 2b), and the remaining signals are specific but of very low abundance
161 (Fig. 2c). Thus, although clone 1H2 is highly-selective when used as an immunoblotting reagent (Fig.
162 2d[5]), it should only be used for the immunofluorescent detection of human RIPK3 under carefully
163 controlled conditions. Our data also showed that clone D6W2T (source: Cell Signaling Technology),
164 an antibody raised against a mark of human RIPK3 activation in necroptosis, phospho-S227,
165 produced specific immunofluorescent signals in paraformaldehyde-fixed cells undergoing
166 necroptosis, but not in methanol-fixed cells (Fig. 2d). Again, the low abundance of these specific
167 immunosignals suggests that clone D6W2T should only be used for immunofluorescence under
168 carefully controlled conditions, such as where *RIPK3*$^{-/-}$ control cells are available for direct
169 comparison. Another caveat is that immunoblotting showed that clone D6W2T not only detected
170 RIPK3 in cells undergoing necroptosis, but also in untreated cells when RIPK3 was presumably not
171 phosphorylated at S227 (Fig. 2d). Therefore, while two of the five antibodies that were tested
172 specifically recognised human RIPK3, the low abundance of their specific signals complicates use of
173 these antibodies for studying endogenous human RIPK3 via immunofluorescence. At present, more
174 specific antibodies are needed to enable the immunofluorescent detection of human RIPK3.
175
176 **Immunofluorescent detection of human RIPK1**
177 We next tested three monoclonal anti-RIPK1 antibodies: one against the N-terminal domain (source:
178 Cell Signaling Technology clone D94C12), one against the C-terminal region (source: BD
179 Transduction Laboratories clone 38/RIP) and one raised against phospho-S166 (source: Cell
180 Signaling Technology clone D8I3A; Fig. 3a). All three clones yielded specific immunofluorescent
181 signals in methanol- and paraformaldehyde-fixed cells, however, these signals were more abundant
182 in methanol-fixed samples (Fig. 3b-d). All three clones were also specific via immunoblot (Fig. 3e).

Importantly, the immunosignals from clones D94C12 and 38/RIP were markedly lower in cells undergoing necroptosis than in unstimulated wild-type cells (Fig. 3d-e). This observation is likely due to RIPK1 undergoing widespread post-translational modification and/or proteasomal degradation during TNF-induced cell death[51, 52]. Thus, despite clones D94C12 and 38/RIP exhibiting a favourable immunostaining profile in unstimulated cells, their decreased reactivity in cells undergoing necroptosis indicates that they should be used judiciously for immunofluorescent labelling of samples for accurate analysis of necroptosis. Conversely, while clone D813A preferentially stains RIPK1 in cells undergoing necroptosis, specific signals that were detected also had low intensity (Fig. 3b) and low abundance (Fig. 3c). In summary, three highly-specific antibodies exist for human RIPK1. However, because their specific signals have very low intensity and abundance in necroptotic cells, their use for the immunofluorescent detection of RIPK1 during necroptosis should be carefully controlled, including side-by-side examination of wild-type and *RIPK1*$^{-/-}$ control cells.

Immunofluorescent detection of mouse MLKL

To our knowledge, there are currently no validated monoclonal antibodies for the immunofluorescent detection for mouse MLKL in unstimulated cells. Accordingly, we raised a monoclonal antibody, clone 5A6 (source: in-house), against full-length mouse MLKL (Fig. 4a). The epitope for clone 5A6 resides in the C-terminal domain of mouse MLKL (Fig. S3). As shown in Fig. 4a-d, clone 5A6 produced specific and abundant signals for endogenous mouse MLKL in methanol-fixed, but not paraformaldehyde-fixed cells. Immunoblotting confirmed that clone 5A6 was highly-specific (Fig. 4e). Notably, compared to human MLKL which translocates en masse into cytoplasmic clusters during necroptosis, the relocation of mouse MLKL into cytoplasmic clusters during necroptosis was more subtle. This observation may relate to the notion that human MLKL is recruited to the necrosome in a more stable manner than mouse MLKL[28].

Phosphorylation of mouse MLKL at S345 is essential for necroptosis in murine cells[37], and therefore many antibodies have been raised against this phosphosite. We tested three commonly-used antibodies (Fig. 4a-e), namely clones: EPR9515(2) (source: Abcam), 7C6.1[39] (source: Millipore MABC1158) and D6E3G (source: Cell Signaling Technology). All three clones yielded specific immunosignals in methanol-fixed cells (Fig. 4c), whereas only clone 7C6.1 was compatible with paraformaldehyde fixation. However, the performance of clone D6E3G was superior to the other anti-phospho-MLKL antibodies, because specific signals were more abundant (Fig. 4c) and represented a higher percentage of the total detectable signal (Fig. 4b). This trend was also evident via immunoblot, with clone 7C6.1 being largely non-specific, clone EPR9515(2) being moderately specific and clone D6E3G exhibiting a high degree of specificity towards activated MLKL in necroptotic cells (Fig. 4e).

In summary, clones 5A6 and D6E3G allow the immunofluorescent detection of mouse MLKL under resting and necroptotic conditions, respectively. Moreover, as with human MLKL, methanol is the fixative of choice for robust immunofluorescent detection of endogenous mouse MLKL.

Immunofluorescent detection of mouse RIPK3

There are numerous well-validated antibodies raised against mouse RIPK3, including a polyclonal antibody against the C-terminus (source: ProSci 2283), and monoclonal antibodies recognising phospho-T231/phospho-S232 (source: Genentech clone GEN135-35-9[53]) and the extended kinase domain (residues 2-353) of mouse RIPK3 (clone 8G7[5], in-house; Fig. 5a). These antibodies yielded specific signals via both immunofluorescence and immunoblot analyses (Fig. 5b-e). Interestingly, while phospho-RIPK3 concentrates into cytoplasmic clusters during necroptosis, this relocation event was not detected by other, anti-total RIPK3 antibodies (Fig. 5d). This finding suggests that the epitopes for RIPK3 detection are obscured via protein-protein interactions during the chronology of necroptotic signaling events. To further probe the steps in the pathway, we generated another mouse RIPK3 antibody, clone 1H12 (source: in-house), which has a favourable staining profile (Fig. 5b-c)

and which recognises the translocation of mouse RIPK3 into cytoplasmic clusters during necroptosis (Fig. 5d). Notably, monoclonal antibodies raised against the N-terminal kinase domain of RIPK3, 8G7 and 1H12, detected several species of lower molecular weight than full length RIPK3 by immunoblot. These signals are likely to be spliced isoforms of mouse RIPK3 of varying lengths, each of which harbour the kinase domain antigen (residues 2-353), which are therefore not detected by antibodies directed towards the C-terminus of the full-length mouse RIPK3 isoform, such as ProSci 2283. In summary, there are several excellent options for the immunofluorescent detection of endogenous mouse RIPK3. Notably, unlike MLKL and RIPK1, the choice of fixative has no major bearing on the ability to detect mouse RIPK3 by immunofluorescence (Fig. 5c).

Immunofluorescent detection of mouse RIPK1

RIPK1 exhibits greater sequence identity between mouse and human orthologs than either RIPK3 or MLKL[41]. In keeping with this, both clone D94C12 (source: Cell Signaling Technology) and clone 38/RIP (source: BD Transduction Laboratories), which were raised against human RIPK1, also specifically detected mouse RIPK1 via immunofluorescence and immunoblotting (Fig. 6a-e). A polyclonal antibody raised against phospho-S166 of mouse RIPK1 (31122; source: Cell Signaling Technology) was also found to specifically detect RIPK1 via immunoblot (Fig. 6e) and in methanol-fixed, but not paraformaldehyde-fixed, cells undergoing necroptosis (Fig. 6b-d).

In summary, three highly-specific antibodies exist for mouse RIPK1. However, as was observed in human cells, necroptosis in mouse cells causes a marked reduction in RIPK1 levels (Fig. 6d-e). Thus, the specific immunosignals from the antibodies tested are of low intensity and abundance in necroptotic cells. Therefore, careful gating of signals is recommended for the study of mouse RIPK1 in necroptotic cells.

Antibody cocktails for imaging endogenous necroptotic signaling

Having validated and compared the performance of numerous reagents, we now propose different antibody combinations that can be used to study endogenous necroptotic signaling (Fig. 7a-b). Because these recommendations are made to facilitate the investigation of endogenous necroptotic signaling in fixed cells, we also provide an ImageJ macro to generate signal-to-noise curves for the gating of specific immunosignals (Supplementary File 1). To exemplify the advantages of visualising endogenous necroptotic events *in situ*, we co-stained MDFs for non-phosphorylated MLKL (clone 5A6; source: in-house) and phosphorylated MLKL (clone D6E3G; source: Cell Signaling Technology). Similar to what was described for human MLKL[29], mouse MLKL was observed to concentrate into cytoplasmic clusters during necroptosis. However, this compartmentalisation event is less pronounced than those observed for human MLKL in necroptotic HT29 cells (arrowhead; Fig. 7c). Also similar to what was described for human MLKL[29], phosphorylated MLKL was observed to form focal structures at the plasma membrane, rather than docking uniformly with the cell periphery (Fig. 7c). Remarkably, although smaller than the hotspots of phosphorylated human MLKL that form in necroptotic HT29 cells, junctional accumulations of phosphorylated mouse MLKL were also apparent in necroptotic MDFs (Fig. 7d and Supplementary Video 1). These data suggest that the assembly of both mouse and human MLKL into macromolecular structures at the plasma membrane, and preferentially at sites of intercellular contact, may be an intrinsic and penultimate feature of necroptotic signaling.

DISCUSSION

Here, we profiled the immunofluorescent staining of MLKL, RIPK3 and RIPK1 in fixed human and mouse cells with a panel of 22 antibodies. While 17 of 22 antibodies were capable of detecting their respective necroptotic protein target in fixed wild-type cells and not their knockout counterparts, only 14 of 22 antibodies exhibited favourable signal-to-noise for robust immunostaining (as summarized in Fig. 7a).

The choice of fixative was a critical variable for the immunofluorescent detection of necroptotic proteins. With the exception of phospho-S227 in human RIPK3 and pT231/pS232 in mouse RIPK3, all other epitopes exhibited increased immunoreactivity in methanol-fixed samples. Indeed, immunodetection of MLKL was often found to be entirely contingent upon the use of methanol as a fixative. This observation has ramifications for the experimental and clinical immunohistological detection of cell death, which is almost exclusively performed on aldehyde-fixed samples. Thus, stringent antigen retrieval steps to reverse crosslinks will likely be necessary for the development of a diagnostic assay for necroptosis in patient samples. High resolution microscopy is also mostly performed on aldehyde-fixed cell monolayers. However, as these cell monolayers cannot typically withstand antigen retrieval, we recommend the use of methanol fixation for high resolution immunofluorescence of necroptosis; even though methanol fixation can be sub-optimal for both the retention of certain biomolecules[54] and the preservation of cellular architecture[55, 56]. Indeed, all but one of the antibodies (source: Cell Signaling Technology clone D6W2T) in the suggested toolbox in Fig. 7a are compatible with methanol fixation.

Our data underscore the importance of using controlled experimental conditions to maximise the identification of specific immunosignals. To this end, we used wild-type cells that express high levels of MLKL, RIPK3 and RIPK1, and which have a well-characterised response to necroptotic stimuli. If possible, cell cultures should be fixed when low, but measurable, levels of necroptotic death are occurring (Fig. S1). This is because end-stage dead cells are often lost during/after methanol fixation, and because the immunosignals for phospho-RIPK1, phospho-RIPK3 and phospho-MLKL peak prior to cell death[29]. Notably, the use of knockout cells (for non-phospho-targets) or unstimulated wild-type cells (for phospho-sites) as a negative control is critical, as it provides the information needed to define the signal-to-noise profile of an antibody (Fig. 1b). Additionally, it is also helpful if different antibodies directed toward the same target yield concordant immunofluorescent signals, and if accompanying immunoblot data confirm their specificity. This

combined approach was important for deducing that clone D6E3G (source: Cell Signaling Technology) is the best option for detecting phospho-MLKL in mouse cells (Fig. 4).

It is concerning that the specificity of some antibodies could not be verified. For instance, while numerous studies use the ProSci 2283 antibody to detect human RIPK3[57, 58, 59], we found that it only recognised mouse RIPK3. Similarly, M6697 (source: Sigma-Aldrich) and clone 7C6.1 (source: Millipore) have been widely used to respectively detect human MLKL and mouse MLKL phospho-S345 [39, 60, 61, 62, 63, 64, 65], however these reagents exhibited a low degree of specificity in our hands. Nonetheless, as we did not exhaustively test the performance of these antibodies for immunofluorescence using a wide variety of fixatives, blocking agents, and detergents, we cannot categorically state that they are non-selective. Moreover, as ProSci 2283 (reported to detect mouse and human RIPK3) and Sigma-Aldrich M6697 (reported to detect human MLKL) are polyclonal antibodies, batch-to-batch variation may explain differences in their specificity between studies. It is also noteworthy that the majority of monoclonal antibodies that yielded the most abundant and specific signals were raised against recombinant full-length protein or component domains, rather than unfolded partial domains or peptides. We reasoned that epitopes that are exposed in the cellular forms of these proteins would be similarly presented within a folded protein for immune recognition in the host. Phosphosite-specific antibodies differ in this regard; these were raised using linear phosphopeptides and their specificity likely reflects the unstructured and solvent-exposed nature of the sequences in which they reside.

Broadly, the specific immunosignals described in this study provide consensus about three key compartmentalisation events that underlie necroptotic signaling[66]. First, the core necroptotic proteins - MLKL, RIPK3 and RIPK1 - predominantly reside in the cytosol under basal conditions. Interestingly, rather than being diffusely distributed across the cytosol, this necroptotic machinery exists as small puncta that are below the resolution limit of conventional light microscopy. It may be that these necroptotic proteins are preassembled into a membrane-less organelle under basal

conditions. Second, RIPK1, RIPK3 and MLKL then coalesce into large cytoplasmic clusters. These clusters preferentially locate to the perinuclear space and are necrosome-related as they co-stain for the presence of phospho-RIPK1, -RIPK3 and -MLKL (Fig. 1-7 and ref.[29]). It is important to note that the formation of these necrosomal clusters in TSI-treated HT29 cells occurs subsequent to the phosphorylation of MLKL[29]. While these clusters likely represent a higher-order form of the necrosome, the mechanisms that govern cluster formation and limit their overall size are currently unknown. Third, as necroptotic signaling continues, phospho-MLKL is actively trafficked away from the clusters towards the plasma membrane[26] where it accumulates into supramolecular assemblies called "hotspots"[29]. Recent findings suggest the release of phospho-MLKL from clusters arises from MLKL undergoing a conformational change that accompanies disengagement from necrosomal RIPK3[40]. Our data support such a disengagement step because neither RIPK1 nor RIPK3 were observed to accumulate at the plasma membrane during necroptosis in mouse or human cells (Fig. 2-3 and 5-6). This disengagement step, and formation of supramolecular assemblies by both mouse and human MLKL at the plasma membrane, are likely to be two additional checkpoints in necroptotic signaling.

METHODS

Materials – Primary antibodies and the dilutions used for immunoblotting/immunofluorescence were: rat anti-human MLKL (clone 10C2; produced in-house[29]; 1:2000/1:400), rat anti-human MLKL (clone 7G2; produced in-house[29]; 1:2000/1:400), rabbit anti-phospho-S358 human MLKL (Abcam ab187091; clone EPR9514; 1:2000/1:200), rat anti-mouse, human, rat, horse MLKL (clone 3H1; produced in-house[37] and available as Millipore MABC604; 1:2000/ N/A), mouse anti-phospho-T357 human MLKL (Novus Biological MAB9187; clone 954702; 1:1000/1:200), rabbit anti-human MLKL (Sigma-Aldrich M6697; 1:1000/1:200), rabbit anti-RIPK3 (ProSci #2283; 1:1000/1:200), rabbit anti-human RIPK3 (Novus Biological NBP2-24588; 1:1000/1:200), mouse anti-human RIPK3

(Novus Biological; clone 780115; 1:1000/1:200), rat anti-human RIPK3 (clone 1H2; produced in-house[5] and available as Millipore MABC1640; 1:2000/1:400), rabbit anti-phospho-S227 human RIPK3 (Cell Signaling Technology; clone D6W2T; 1:2000/1:200), rabbit anti-mouse or human RIPK1 (Cell Signaling Technology; clone D94C12; 1:2000/1:200), mouse anti-mouse or human RIPK1 (BD Biosciences; clone 38/RIP; 1:1000/1:100), rabbit anti-phospho-S166 human RIPK1 (Cell Signaling Technology; clone D8I3A; 1:2000/1:200), rat anti-mouse MLKL (clone 5A6; produced in-house), rabbit anti-phospho-S345 mouse MLKL (Abcam; clone EPR9515(2); 1:2000/1:200), mouse anti-phospho-S345 mouse MLKL (Millipore MABC158; clone 7C6.1; 1:2000/1:200), rabbit anti-phospho-S345 mouse MLKL (Cell Signaling Technology; clone D6E3G; 1:2000/1:200), rat anti-mouse RIPK3 (clone 8G7; produced in-house[5] and available from Millipore as MABC1595; 1:2000/1:400), rat anti-mouse RIPK3 (clone 1H12; produced in-house; 1:2000/1:400), rabbit anti-phospho-T231/S232 mouse RIPK3 (Genentech; clone GEN135-35-9[53]; 1:2000/1:400), rabbit anti-phospho-S166 mouse RIPK1 (Cell Signaling Technology 31122; 1:2000/1:200), mouse anti-GAPDH (Millipore MAB374; 1:2000/N/A). Secondary antibodies for immunoblotting were: horseradish peroxidase (HRP)-conjugated goat anti-rat IgG (Southern Biotech 3010-05), HRP-conjugated goat anti-mouse IgG (Southern Biotech 1010-05), and HRP-conjugated goat anti-rabbit IgG (Southern Biotech 4010-05). All secondary antibodies for immunoblotting were used at a dilution of 1:10000. Secondary immunofluorescence detection reagents were: AlexaFluor647-conjugated donkey anti-rabbit IgG (ThermoFisher Scientific A31573), AlexaFluor568-conjugated donkey anti-rabbit IgG (ThermoFisher Scientific A10042), AlexaFluor568-conjugated donkey anti-mouse IgG (ThermoFisher Scientific A10037), AlexaFluor-594 donkey anti-rat IgG (ThermoFisher Scientific A-21209), AlexaFluor488-conjugated donkey anti-rat IgG (ThermoFisher Scientific A21208). All secondary antibodies for immunofluorescence were used at a dilution of 1:1000. Bond-Breaker TCEP solution (ThermoFisher Scientific 77720). *N*-Ethylmaleimide (Sigma-Aldrich E3876).

382 ***5A6 and 1H12 antibody production*** – Antibodies were generated at the Walter and Eliza Hall
383 Institute Monoclonal Antibody Facility by immunizing Wistar rats with recombinant full-length
384 mouse MLKL[37] for clone 5A6 or recombinant mouse RIPK3 residues 2-353 for clone 1H12 and the
385 previously-reported clone 8G7[5] that was expressed and purified from Sf21 insect cells using the
386 baculovirus expression system, before splenocytes were fused with SP2/O mouse myeloid cells and
387 arising hybridoma lines cloned. The specificity of clone 5A6 for mouse MLKL was validated via
388 immunoblot analyses as exemplified in Fig. 4e and Fig. S3. The specificity of clone 1H12 for mouse
389 RIPK3 was validated via immunoblot analyses as exemplified in Fig. 5e.
390
391 ***Cell lines*** – HT29 cells were provided by Mark Hampton (University of Otago). *RIPK1*$^{-/-}$, *RIPK3*$^{-/-}$
392 and *MLKL*$^{-/-}$ HT29 cells have been previously reported[28, 29, 67]. MDF lines were generated in-house
393 from the tails of wild-type C57BL/6J, *Mlkl*$^{-/-}$[37] and *Ripk3*$^{-/-}$[68] mice and immortalized by SV40 large T
394 antigen as reported previously[35, 37]. The sex and precise age of these animals were not recorded,
395 although our MDFs are routinely derived from tails from 8-week-old mice. *Mlkl*$^{-/-}$*Ripk1*$^{-/-}$ MDFs were
396 derived from the belly/back dermis of *Mlkl*$^{-/-}$*Ripk1*$^{-/-}$ E19.5 mice[16] and immortalized as described
397 above. MDF lines were generated in accordance with protocols approved by the Walter and Eliza
398 Hall Institute of Medical Research Animal Ethics Committee. Cell line identities were not further
399 validated, although their morphologies and responses to necroptotic stimuli were consistent with their
400 stated origins. Cell lines were routinely monitored to confirm they were mycoplasma-free.
401
402 ***Cell culture*** – HT29 cells were maintained in Dulbecco's Modified Eagle Medium (DMEM; Life
403 Technologies) containing 8% v/v heat-inactivated fetal calf serum (FCS), 2 mM L-Glutamine/-
404 GlutaMAX (ThermoFisher Scientific 35050061), 50 U ml^{-1} penicillin and 50 U ml^{-1} streptomycin
405 (G/P/S) under humidified 10% CO_2 at 37°C.
406

Cell Treatment – Cells were seeded into Ibi-treated 8-well μ-slides (Ibidi 80826) in media containing 8% v/v FCS and G/P/S at 3.0×10^4 cells per well for HT29 and 0.25×10^4 cells per well for MDFs. Cells were left to adhere overnight then treated in media containing 1% v/v FCS and G/P/S and supplemented with the following stimuli: 100ng/mL recombinant human TNF-α-Fc (produced in-house as in ref.[69]), 500nM Smac mimetic/Compound A (provided by Tetralogic Pharmaceuticals; as in ref.[70]), 5μM IDN-6556 (provided by Tetralogic Pharmaceuticals). Unless stipulated, HT29 cells were stimulated for 7.5 h with TSI and MDF cells were stimulated for 90 min with TSI.

LDH release **–** Colorimetric LDH release assay kit (Promega G1780) was performed according to manufacturer's instructions.

Whole cell lysate, SDS-PAGE, immunoblot & quantification **–** Cells were lysed in ice-cold RIPA buffer (10mM Tris-HCl pH 8.0, 1mM EGTA, 2mM $MgCl_2$, 0.5% v/v Triton X100, 0.1% w/v Na deoxycholate, 0.5% w/v SDS and 90mM NaCl) supplemented with 1x Protease & Phosphatase Inhibitor Cocktail (Cell Signaling Technology 5872S) and 100U/mL Benzonase (Sigma-Aldrich E1014). Whole cell lysates were boiled for 10 minutes in 1× SDS Laemmli sample buffer (126 mM Tris-HCl, pH 8, 20% v/v glycerol, 4% w/v SDS, 0.02% w/v bromophenol blue, 5% v/v 2-mercaptoethanol), and resolved on 1.5mm NuPAGE 4–12% Bis-Tris gels (ThermoFisher Scientific NP0335BOX) using MES Running buffer (ThermoFisher Scientific NP000202) or Bio-Rad Criterion TGX 4-15% gels (Bio-Rad 5678085) using 1x TGS buffer (Bio-Rad 1610772). After transfer onto nitrocellulose, membranes were blocked in 5% w/v skim milk powder in TBS-T, probed with primary antibodies (see ***Materials*** above) then the appropriate HRP-conjugated secondary antibody (see ***Materials*** above) and signals revealed by enhanced chemiluminescence (Merck P90720) on a ChemiDoc Touch Imaging System (Bio-Rad). Between each probe, membranes were incubated in

stripping buffer (200mM glycine pH 2.9, 1% w/v SDS, 0.5mM TCEP) for 30 minutes at room temperature then re-blocked.

Subcellular fractionation, BN-PAGE & immunoblot – HT29 cells or MDFs were seeded into 6-well plates (1.0×10^6 cells per well) in media containing 8% v/v FCS and G/P/S and equilibrated overnight under humidified 10% CO_2 at 37 °C conditions. Cells were then treated in media containing 1% FCS and G/P/S supplemented with the agonists (as indicated above). Cells were fractionated into cytoplasmic and membrane fractions[35]. Cells were permeabilized in MELB buffer (20 mM HEPES pH 7.5, 100 mM KCl, 2.5 mM $MgCl_2$ and 100 mM sucrose, 0.025% v/v digitonin, 2 μM N-ethyl maleimide, phosphatase and protease inhibitors). Crude membrane and cytoplasmic fractions were separated by centrifugation (5 minutes 11,000*g*), and fractions prepared in buffers to a final concentration of 1% w/v digitonin. The samples were resolved on a 4–16% Bis-Tris Native PAGE gel (ThermoFisher), transferred to polyvinylidene difluoride (Merck IPVH00010). After transfer, membranes were destained (in 50% (v/v) methanol, 25% (v/v) acetic acid), denatured (in 6M Guanidine hydrochloride, 10 mM Tris pH6.8, 5 mM β-mercaptoethanol), blocked in 5% skim milk (Diploma), and probed in the same manner as above.

Protein production and purification – Full-length human and mouse MLKL and the C-terminal, pseudokinase domain of mouse and human MLKL were expressed in Sf21 insect cells using the Bac-to-Bac system (ThermoFisher Scientific) and purified using established procedures[28, 37, 42]. Briefly, proteins were expressed with an N-terminal, TEV protease-cleavable GST (full length human MLKL) or His_6 (full length mouse MLKL and pseudokinase domains) tags and captured from lysates using glutathione resin (UBP Bio) or HisTag Ni-NTA resin (Roche) respectively. Proteins were cleaved on-resin from the GST tag or off-resin for His_6 tags using His-tagged TEV protease, before protease was removed by Ni-NTA chromatography (HisTag resin, Roche). Protein was concentrated by

centrifugal ultrafiltration and applied to a Superdex-200 (GE Healthcare) size exclusion chromatography column; protein was eluted in 20 mM HEPES pH 7.5, 200 mM NaCl, 5% v/v glycerol. Protein containing fractions were spin concentrated to 5-10 mg/mL, aliquoted, snap frozen in liquid N_2 and stored at –80ºC until required.

Immunofluorescence **–** Cells in 8-well µ-Slides (Ibidi 80826) were ice-chilled for 3 minutes, then washed in ice-cold Dulbecco's PBS (dPBS; ThermoFisher Scientific 14190144), then fixed for 30 minutes in either ice-cold methanol or ice-cold 4% w/v PFA. Cells were washed twice in ice-cold dPBS, then blocked in ice-cold Tris-balanced salt solution with 0.05% v/v Triton-X100 (TBS-T) supplemented with 10% v/v donkey serum (Sigma-Aldrich D9663) for >1 hour. Cells were incubated in primary antibodies (see ***Materials*** above) overnight at 4 ºC in TBS-T with 10% v/v donkey serum. Cells were washed twice in TBS-T then incubated in the appropriate secondary antibodies supplemented with 0.1µg/mL Hoechst 33342 (ThermoFisher Scientific H3570) for 3 hours at room temperature with gentle rocking. Cells were washed four times in ice-cold TBS-T then stored at 4 ºC until imaged. Where indicated, to demarcate the plasma membrane, 2µL of biotinylated wheat germ agglutinin (Sigma-Aldrich L5142) was added to each well 10 minutes before fixation. The fixed wheat germ agglutinin was then detected via the addition of 1:1000 dilution of DyLight650-conjugated streptavidin (ThermoFisher Scientific 84547) during the secondary antibody incubation step.

Two-dimensional epifluorescence microscopy - Samples in TBS-T were imaged on an Inverted Axio Observer.Z1 microscope (Zeiss) with the following specifications: C-Apochromat 40x/1.20 W autocorr UV VIS IR lens, HXP 120V excitation source, AlexaFluor647 and DyLight650 imaged with a $\lambda_{Excitation}$=625-655nm; $\lambda_{beamsplitter}$=660nm; $\lambda_{Emission}$=665-715nm filter, AlexaFluor568 imaged with a $\lambda_{Excitation}$=532-544nm; $\lambda_{beamsplitter}$=560nm; $\lambda_{Emission}$=573-613nm, AlexaFluor488 imaged with a

481 $\lambda_{Excitation}$=450-490nm; $\lambda_{beamsplitter}$=495nm; $\lambda_{Emission}$=500-550nm, Hoechst 33342 imaged with a
482 $\lambda_{Excitation}$=359-371nm; $\lambda_{beamsplitter}$=395nm; $\lambda_{Emission}$=397-∞ nm, a sCMOS PCO.edge 4.2 camera, ZEN
483 blue 2.5 pro capture software and ImageJ 1.53c post-acquisition processing software[71]. Typically, for
484 each independent experiment, 5-10 randomly selected fields were captured per treatment group,
485 whereby only the Hoechst 33342 signal was visualised prior to multi-channel acquisition. To ensure
486 consistent signal intensities across independent experiments, the same excitation, emission and
487 camera settings were used throughout this study.
488
489 ***Airyscan microscopy*** – Fixed immunostained cells in 8-well μ-Slides (Ibidi 80827) were subjected
490 to super-resolution 3-dimensional Airyscan microscopy on an Inverted LSM 880 platform (Zeiss)
491 equipped with the following specifications: a 63x/1.4 N.A. PlanApo DIC M27 oil immersion
492 objective (Zeiss), 405-, 488-, 568- and 640-nm laser lines, and radially-stacked Airyscan GaASP
493 detectors set to SR-mode, 405-, 488-, 561-, 633-nm laser lines and ZEN black 2.3 SP1 FP3 v14.0
494 capture software. Image stacks were acquired with a z-step size of 159nm. Super-resolution
495 deconvolution was performed using the automated '3D AiryScan Processing' function of ZEN blue
496 software.
497
498 ***Hotspot quantitation*** – Micrographs (captured as in ***two-dimensional epifluorescence microscopy***)
499 were opened in ImageJ 1.53c[71]. A rolling ball filter of 7 was applied and phospho-S358 MLKL
500 immunosignals thresholded (≥7000 units) and objects segmented using the 'Analyze>Analyze
501 Particles' tool. Segmented objects with size 0.5-100μm^2 and feret diameter>2 (i.e. elliptical objects)
502 were considered hotspots. The number of segmented objects per 100 cells was taken as an index of
503 hotspot occurrence. The mean size of the segmented objects was taken as an index of hotspot size.
504 The fluorescence intensity of each segmented object divided by its size was taken as an index of
505 hotspot intensity.

ACKNOWLEDGEMENTS

We thank the Walter and Eliza Hall Institute Monoclonal Antibody Facility for their assistance generating clones 3H1, 10C2, 7G2, 1H2, 5A6, 8G7 and 1H12; and Cathrine Hall for assistance generating *Mlkl*$^{-/-}$ *Ripk1*$^{-/-}$ MDF lines. We are grateful to the Australian National Health and Medical Research Council for fellowship (J.M.H., 1142669; E.D.H., 1159488; J.M.M., 1172929), grant (1124735, 1124737, and 1105023), and infrastructure (IRIISS 9000587) support, with additional support from the CASS Foundation (A.L.S.) and the Victorian Government Operational Infrastructure Support scheme. We acknowledge the support for A.V.J. from an Australian Research Training Program Scholarship.

AUTHOR CONTRIBUTIONS

Investigation: A.L.S., K.P., C.F., J.M.H., L.W., J.R., A.V.J., C.R.H., X.G., S.N.Y. Supervision and Methodology: A.L.S., J.M.H., K.L.R., E.D.H. and J.M.M.; Conceptualization: A.L.S., E.D.H. and J.M.M.; Writing – Original Draft: A.L.S. and J.M.M.; Writing – Review & Editing: all authors.

COMPETING INTERESTS

A.L.S., K.P. C.F., J.M.H., S.N.Y. and J.M.M. contribute to a project developing necroptosis inhibitors in collaboration with Anaxis Pharma. The other authors declare no competing interests.

MATERIALS REQUESTS

All materials will be provided under Materials Transfer Agreement upon request to James Murphy (jamesm@wehi.edu.au).

REFERENCES

1. Cho YS, Challa S, Moquin D, Genga R, Ray TD, Guildford M*, et al.* Phosphorylation-driven assembly of the RIP1-RIP3 complex regulates programmed necrosis and virus-induced inflammation. *Cell* 2009, **137**(6)**:** 1112-1123.

2. Guo H, Omoto S, Harris PA, Finger JN, Bertin J, Gough PJ*, et al.* Herpes simplex virus suppresses necroptosis in human cells. *Cell Host Microbe* 2015, **17**(2)**:** 243-251.

3. Pearson JS, Giogha C, Muhlen S, Nachbur U, Pham CL, Zhang Y*, et al.* EspL is a bacterial cysteine protease effector that cleaves RHIM proteins to block necroptosis and inflammation. *Nat Microbiol* 2017, **2:** 16258.

4. Pearson JS, Murphy JM. Down the rabbit hole: Is necroptosis truly an innate response to infection? *Cell Microbiol* 2017, **19**(8)**:** e12750.

5. Petrie EJ, Sandow JJ, Lehmann WIL, Liang LY, Coursier D, Young SN*, et al.* Viral MLKL Homologs Subvert Necroptotic Cell Death by Sequestering Cellular RIPK3. *Cell reports* 2019, **28**(13)**:** 3309-3319 e3305.

6. Fletcher-Etherington A, Nobre L, Nightingale K, Antrobus R, Nichols J, Davison AJ*, et al.* Human cytomegalovirus protein pUL36: A dual cell death pathway inhibitor. *Proc Natl Acad Sci U S A* 2020, **117**(31)**:** 18771-18779.

7. Kitur K, Wachtel S, Brown A, Wickersham M, Paulino F, Penaloza HF*, et al.* Necroptosis Promotes Staphylococcus aureus Clearance by Inhibiting Excessive Inflammatory Signaling. *Cell reports* 2016, **16**(8)**:** 2219-2230.

8. Shubina M, Tummers B, Boyd DF, Zhang T, Yin C, Gautam A*, et al.* Necroptosis restricts influenza A virus as a stand-alone cell death mechanism. *J Exp Med* 2020, **217**(11).

9. Simpson J, Loh Z, Ullah MA, Lynch JP, Werder RB, Collinson N*, et al.* Respiratory Syncytial Virus Infection Promotes Necroptosis and HMGB1 Release by Airway Epithelial Cells. *Am J Respir Crit Care Med* 2020, **201**(11)**:** 1358-1371.

10. Muller T, Dewitz C, Schmitz J, Schroder AS, Brasen JH, Stockwell BR, *et al.* Necroptosis and ferroptosis are alternative cell death pathways that operate in acute kidney failure. *Cell Mol Life Sci* 2017, **74**(19)**:** 3631-3645.

11. Pefanis A, Ierino FL, Murphy JM, Cowan PJ. Regulated necrosis in kidney ischemia-reperfusion injury. *Kidney Int* 2019, **96**(2)**:** 291-301.

12. Luedde M, Lutz M, Carter N, Sosna J, Jacoby C, Vucur M, *et al.* RIP3, a kinase promoting necroptotic cell death, mediates adverse remodelling after myocardial infarction. *Cardiovasc Res* 2014, **103**(2)**:** 206-216.

13. Hildebrand JM, Kauppi M, Majewski IJ, Liu Z, Cox AJ, Miyake S, *et al.* A missense mutation in the MLKL brace region promotes lethal neonatal inflammation and hematopoietic dysfunction. *Nat Commun* 2020, **11**(1)**:** 3150.

14. Wang H, Sun L, Su L, Rizo J, Liu L, Wang LF, *et al.* Mixed Lineage Kinase Domain-like Protein MLKL Causes Necrotic Membrane Disruption upon Phosphorylation by RIP3. *Mol Cell* 2014, **54**(1)**:** 133-146.

15. Rickard JA, Anderton H, Etemadi N, Nachbur U, Darding M, Peltzer N, *et al.* TNFR1-dependent cell death drives inflammation in Sharpin-deficient mice. *Elife* 2014, **3:** e03464.

16. Rickard JA, O'Donnell JA, Evans JM, Lalaoui N, Poh AR, Rogers TW, *et al.* RIPK1 regulates RIPK3-MLKL driven systemic inflammation and emergency hematopoiesis. *Cell* 2014, **157**(2)**:** 1175-1188.

17. Pierdomenico M, Negroni A, Stronati L, Vitali R, Prete E, Bertin J, *et al.* Necroptosis is active in children with inflammatory bowel disease and contributes to heighten intestinal inflammation. *Am J Gastroenterol* 2014, **109**(2)**:** 279-287.

18. He S, Wang L, Miao L, Wang T, Du F, Zhao L, *et al.* Receptor interacting protein kinase-3 determines cellular necrotic response to TNF-alpha. *Cell* 2009, **137**(6)**:** 1100-1111.

19. Zhang DW, Shao J, Lin J, Zhang N, Lu BJ, Lin SC, *et al.* RIP3, an energy metabolism regulator that switches TNF-induced cell death from apoptosis to necrosis. *Science* 2009, **325**(5938)**:** 332-336.

20. Sun L, Wang H, Wang Z, He S, Chen S, Liao D, *et al.* Mixed lineage kinase domain-like protein mediates necrosis signaling downstream of RIP3 kinase. *Cell* 2012, **148**(1-2)**:** 213-227.

21. Zhao J, Jitkaew S, Cai Z, Choksi S, Li Q, Luo J, *et al.* Mixed lineage kinase domain-like is a key receptor interacting protein 3 downstream component of TNF-induced necrosis. *Proc Natl Acad Sci U S A* 2012, **109**(14)**:** 5322-5327.

22. Wang T, Perera ND, Chiam MDF, Cuic B, Wanniarachchillage N, Tomas D, *et al.* Necroptosis is dispensable for motor neuron degeneration in a mouse model of ALS. *Cell Death Differ* 2019.

23. Dermentzaki G, Politi KA, Lu L, Mishra V, Perez-Torres EJ, Sosunov AA, *et al.* Deletion of Ripk3 Prevents Motor Neuron Death In Vitro but not In Vivo. *eNeuro* 2019, **6**(1).

24. Dominguez S, Varfolomeev E, Brendza R, Stark K, Tea J, Imperio J, *et al.* Genetic inactivation of RIP1 kinase does not ameliorate disease in a mouse model of ALS. *Cell Death Differ* 2020.

25. Dara L, Johnson H, Suda J, Win S, Gaarde W, Han D, *et al.* Receptor interacting protein kinase 1 mediates murine acetaminophen toxicity independent of the necrosome and not through necroptosis. *Hepatology* 2015, **62**(6)**:** 1847-1857.

26. Petrie EJ, Birkinshaw RW, Koide A, Denbaum E, Hildebrand JM, Garnish SE, *et al.* Identification of MLKL membrane translocation as a checkpoint in necroptotic cell death using Monobodies. *Proc Natl Acad Sci U S A* 2020, **117**(15)**:** 8468-8475.

27. Petrie EJ, Czabotar PE, Murphy JM. The Structural Basis of Necroptotic Cell Death Signaling. *Trends Biochem Sci* 2019, **44**(1)**:** 53-63.

28. Petrie EJ, Sandow JJ, Jacobsen AV, Smith BJ, Griffin MDW, Lucet IS, *et al.* Conformational switching of the pseudokinase domain promotes human MLKL tetramerization and cell death by necroptosis. *Nat Commun* 2018, **9**(1)**:** 2422.

29. Samson AL, Zhang Y, Geoghegan ND, Gavin XJ, Davies KA, Mlodzianoski MJ, *et al.* MLKL trafficking and accumulation at the plasma membrane control the kinetics and threshold for necroptosis. *Nat Commun* 2020, **11**(1)**:** 3151.

30. Li J, McQuade T, Siemer AB, Napetschnig J, Moriwaki K, Hsiao YS, *et al.* The RIP1/RIP3 necrosome forms a functional amyloid signaling complex required for programmed necrosis. *Cell* 2012, **150**(2)**:** 339-350.

31. Mompean M, Li W, Li J, Laage S, Siemer AB, Bozkurt G, *et al.* The Structure of the Necrosome RIPK1-RIPK3 Core, a Human Hetero-Amyloid Signaling Complex. *Cell* 2018, **173**(5)**:** 1244-1253 e1210.

32. Sun X, Yin J, Starovasnik MA, Fairbrother WJ, Dixit VM. Identification of a novel homotypic interaction motif required for the phosphorylation of receptor-interacting protein (RIP) by RIP3. *J Biol Chem* 2002, **277**(11)**:** 9505-9511.

33. Cook WD, Moujalled DM, Ralph TJ, Lock P, Young SN, Murphy JM, *et al.* RIPK1- and RIPK3-induced cell death mode is determined by target availability. *Cell Death Differ* 2014, **21**(10)**:** 1600-1612.

34. Orozco S, Yatim N, Werner MR, Tran H, Gunja SY, Tait SW, *et al.* RIPK1 both positively and negatively regulates RIPK3 oligomerization and necroptosis. *Cell Death Differ* 2014, **21**(10)**:** 1511-1521.

35. Hildebrand JM, Tanzer MC, Lucet IS, Young SN, Spall SK, Sharma P, *et al.* Activation of the pseudokinase MLKL unleashes the four-helix bundle domain to induce membrane localization and necroptotic cell death. *Proc Natl Acad Sci U S A* 2014, **111**(42)**:** 15072-15077.

36. Murphy JM. The Killer Pseudokinase Mixed Lineage Kinase Domain-Like Protein (MLKL). *Cold Spring Harb Perspect Biol* 2020, **12**(8).

37. Murphy JM, Czabotar PE, Hildebrand JM, Lucet IS, Zhang JG, Alvarez-Diaz S*, et al.* The pseudokinase MLKL mediates necroptosis via a molecular switch mechanism. *Immunity* 2013, **39**(3)**:** 443-453.

38. Tanzer MC, Tripaydonis A, Webb AI, Young SN, Varghese LN, Hall C*, et al.* Necroptosis signalling is tuned by phosphorylation of MLKL residues outside the pseudokinase domain activation loop. *The Biochemical journal* 2015, **471**(2)**:** 255-265.

39. Rodriguez DA, Weinlich R, Brown S, Guy C, Fitzgerald P, Dillon CP*, et al.* Characterization of RIPK3-mediated phosphorylation of the activation loop of MLKL during necroptosis. *Cell Death Differ* 2016, **23**(1)**:** 76-88.

40. Garnish SE, Meng Y, Koide A, Sandow JJ, Denbaum E, Jacobsen AV*, et al.* Conformational interconversion of MLKL and disengagement from RIPK3 precedes cell death by necroptosis. Under review.

41. Davies KA, Fitzgibbon C, Young SN, Garnish SE, Yeung W, Coursier D*, et al.* Distinct pseudokinase domain conformations underlie divergent activation mechanisms among vertebrate MLKL orthologues. *Nat Commun* 2020, **11**(1)**:** 3060.

42. Murphy JM, Lucet IS, Hildebrand JM, Tanzer MC, Young SN, Sharma P*, et al.* Insights into the evolution of divergent nucleotide-binding mechanisms among pseudokinases revealed by crystal structures of human and mouse MLKL. *The Biochemical journal* 2014, **457**(3)**:** 369-377.

43. Tanzer MC, Matti I, Hildebrand JM, Young SN, Wardak A, Tripaydonis A*, et al.* Evolutionary divergence of the necroptosis effector MLKL. *Cell Death Differ* 2016, **23**(7)**:** 1185-1197.

44. Davies KA, Tanzer MC, Griffin MDW, Mok YF, Young SN, Qin R*, et al.* The brace helices of MLKL mediate interdomain communication and oligomerisation to regulate cell death by necroptosis. *Cell Death Differ* 2018, **25**(9)**:** 1567-1580.

45. Dondelinger Y, Hulpiau P, Saeys Y, Bertrand MJM, Vandenabeele P. An evolutionary perspective on the necroptotic pathway. *Trends Cell Biol* 2016, **26**(10)**:** 721-732.

46. Newton K, Manning G. Necroptosis and Inflammation. *Annu Rev Biochem* 2016, **85:** 743-763.

47. Petrie EJ, Birkinshaw RW, Koide A, Denbaum E, Hildebrand JM, Garnish SE*, et al.* Identification of MLKL membrane translocation as a checkpoint in necroptotic cell death using Monobodies. *Proc Natl Acad Sci U S A* 2020.

48. Wang H, Sun L, Su L, Rizo J, Liu L, Wang LF*, et al.* Mixed lineage kinase domain-like protein MLKL causes necrotic membrane disruption upon phosphorylation by RIP3. *Mol Cell* 2014, **54**(1)**:** 133-146.

49. Cai Z, Jitkaew S, Zhao J, Chiang HC, Choksi S, Liu J*, et al.* Plasma membrane translocation of trimerized MLKL protein is required for TNF-induced necroptosis. *Nature cell biology* 2014, **16**(1)**:** 55-65.

50. Chen X, Li W, Ren J, Huang D, He WT, Song Y*, et al.* Translocation of mixed lineage kinase domain-like protein to plasma membrane leads to necrotic cell death. *Cell research* 2014, **24**(1)**:** 105-121.

51. Alturki NA, McComb S, Ariana A, Rijal D, Korneluk RG, Sun SC*, et al.* Triad3a induces the degradation of early necrosome to limit RipK1-dependent cytokine production and necroptosis. *Cell Death Dis* 2018, **9**(6)**:** 592.

52. Simpson DS, Gabrielyan A, Feltham R. RIPK1 ubiquitination: Evidence, correlations and the undefined. *Semin Cell Dev Biol* 2020.

53. Newton K, Wickliffe KE, Maltzman A, Dugger DL, Strasser A, Pham VC, *et al.* RIPK1 inhibits ZBP1-driven necroptosis during development. *Nature* 2016, **540**(7631)**:** 129-133.

54. Hoetelmans RW, Prins FA, Cornelese-ten Velde I, van der Meer J, van de Velde CJ, van Dierendonck JH. Effects of acetone, methanol, or paraformaldehyde on cellular structure, visualized by reflection contrast microscopy and transmission and scanning electron microscopy. *Appl Immunohistochem Mol Morphol* 2001, **9**(4)**:** 346-351.

55. Moloney M, McDonnell L, O'Shea H. Atomic force microscopy of BHK-21 cells: an investigation of cell fixation techniques. *Ultramicroscopy* 2004, **100**(3-4)**:** 153-161.

56. Whelan DR, Bell TD. Correlative Synchrotron Fourier Transform Infrared Spectroscopy and Single Molecule Super Resolution Microscopy for the Detection of Composition and Ultrastructure Alterations in Single Cells. *ACS Chem Biol* 2015, **10**(12)**:** 2874-2883.

57. Xu X, Kalac M, Markson M, Chan M, Brody JD, Bhagat G, *et al.* Reversal of CYLD phosphorylation as a novel therapeutic approach for adult T-cell leukemia/lymphoma (ATLL). *Cell Death Dis* 2020, **11**(2)**:** 94.

58. Yang C, Li J, Yu L, Zhang Z, Xu F, Jiang L, *et al.* Regulation of RIP3 by the transcription factor Sp1 and the epigenetic regulator UHRF1 modulates cancer cell necroptosis. *Cell Death Dis* 2017, **8**(10)**:** e3084.

59. Wang S, Ni HM, Dorko K, Kumer SC, Schmitt TM, Nawabi A, *et al.* Increased hepatic receptor interacting protein kinase 3 expression due to impaired proteasomal functions contributes to alcohol-induced steatosis and liver injury. *Oncotarget* 2016, **7**(14)**:** 17681-17698.

60. Zhang S, Che L, He C, Huang J, Guo N, Shi J, *et al.* Drp1 and RB interaction to mediate mitochondria-dependent necroptosis induced by cadmium in hepatocytes. *Cell Death Dis* 2019, **10**(7)**:** 523.

61. Ali M, Mocarski ES. Proteasome inhibition blocks necroptosis by attenuating death complex aggregation. *Cell Death Dis* 2018, **9**(3)**:** 346.

62. Gong YN, Guy C, Olauson H, Becker JU, Yang M, Fitzgerald P, *et al.* ESCRT-III Acts Downstream of MLKL to Regulate Necroptotic Cell Death and Its Consequences. *Cell* 2017, **169**(2)**:** 286-300 e216.

63. Yoon S, Bogdanov K, Kovalenko A, Wallach D. Necroptosis is preceded by nuclear translocation of the signaling proteins that induce it. *Cell Death Differ* 2016, **23**(2)**:** 253-260.

64. Wang Z, Jiang H, Chen S, Du F, Wang X. The mitochondrial phosphatase PGAM5 functions at the convergence point of multiple necrotic death pathways. *Cell* 2012, **148**(1-2)**:** 228-243.

65. Mizumura K, Cloonan SM, Nakahira K, Bhashyam AR, Cervo M, Kitada T, *et al.* Mitophagy-dependent necroptosis contributes to the pathogenesis of COPD. *J Clin Invest* 2014, **124**(9)**:** 3987-4003.

66. Samson AL, Garnish SE, Hildebrand JM, Murphy JM. Location, location, location: a compartmentalized view of necroptotic signaling. Under review.

67. Tanzer MC, Khan N, Rickard JA, Etemadi N, Lalaoui N, Spall SK, *et al.* Combination of IAP antagonist and IFNgamma activates novel caspase-10- and RIPK1-dependent cell death pathways. *Cell Death Differ* 2017, **24**(3)**:** 481-491.

68. Newton K, Sun X, Dixit VM. Kinase RIP3 is dispensable for normal NF-kappa Bs, signaling by the B-cell and T-cell receptors, tumor necrosis factor receptor 1, and Toll-like receptors 2 and 4. *Mol Cell Biol* 2004, **24**(4)**:** 1464-1469.

69. Bossen C, Ingold K, Tardivel A, Bodmer JL, Gaide O, Hertig S, *et al.* Interactions of tumor necrosis factor (TNF) and TNF receptor family members in the mouse and human. *J Biol Chem* 2006, **281**(20)**:** 13964-13971.

70. Vince JE, Wong WW, Khan N, Feltham R, Chau D, Ahmed AU, *et al.* IAP antagonists target cIAP1 to induce TNFalpha-dependent apoptosis. *Cell* 2007, **131**(4)**:** 682-693.

797 71. Schneider CA, Rasband WS, Eliceiri KW. NIH Image to ImageJ: 25 years of image analysis.
798 *Nat Methods* 2012, **9**(7)**:** 671-675.

799

800

FIGURES LEGENDS

Figure 1

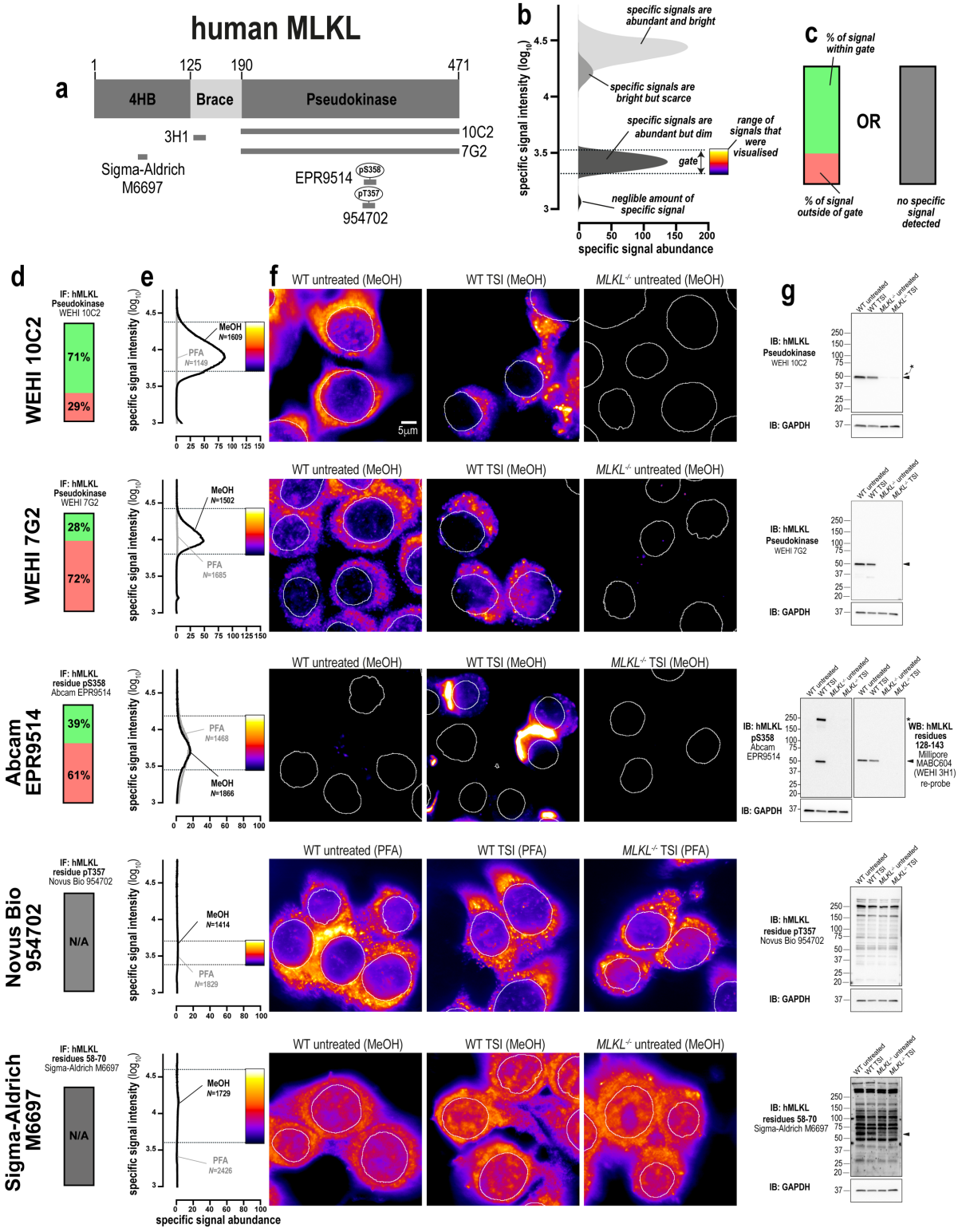

Figure 1: Methanol fixation is optimal for the immunofluorescent detection of human MLKL

a Human MLKL domain architecture showing the immunogens used to raise the tested anti-MLKL antibodies. **b** Demonstration of how signal-to-noise ratios were used to quantify the abundance and brightness of specific immunofluorescent signals generated by different antibodies. The 5th and 95th percentile of each signal-to-noise curve defines the gate where specific immunosignals were observed. As indicated by the pseudocolour look-up-table, only immunosignals within this gate were visualised. **c** Chart exemplifying how the amount of signal within the gate, relative to the total amount of detectable signal, provides another gauge of antibody specificity for immunofluorescence. **d** Quantitation of the percentage of gated signals for the tested MLKL antibodies. **e** Quantitation of specific signal abundance produced by the tested MLKL antibodies on methanol-fixed (MeOH) or paraformaldehyde-fixed (PFA) HT29 cells. The number of cells imaged (N) to generate each signal-to-noise curve is shown. **f** Micrographs of immunofluorescent signals for the tested MLKL antibodies on HT29 cells. As indicated by each pseudocolour look-up-table, only immunosignals within the respective gate in panel **e** were visualised. Data are representative of n=3 (clones 10C2, 7G2) and n=2 (Abcam clone EPR9514, Novus Biological MAB9187/clone 954702 and Sigma-Aldrich M6697) independent experiments. Nuclei were detected by Hoechst 33342 staining and are demarked by white outlines in micrographs. **g** Immunoblot using the tested MLKL antibodies against wild-type and *MLKL*$^{-/-}$ HT29 cell lysates. Closed arrowheads indicate the main specific band. Asterisks indicate non-specific bands that could otherwise confound data interpretation. Immunoblots were re-probed for GAPDH as loading control.

Figure 2

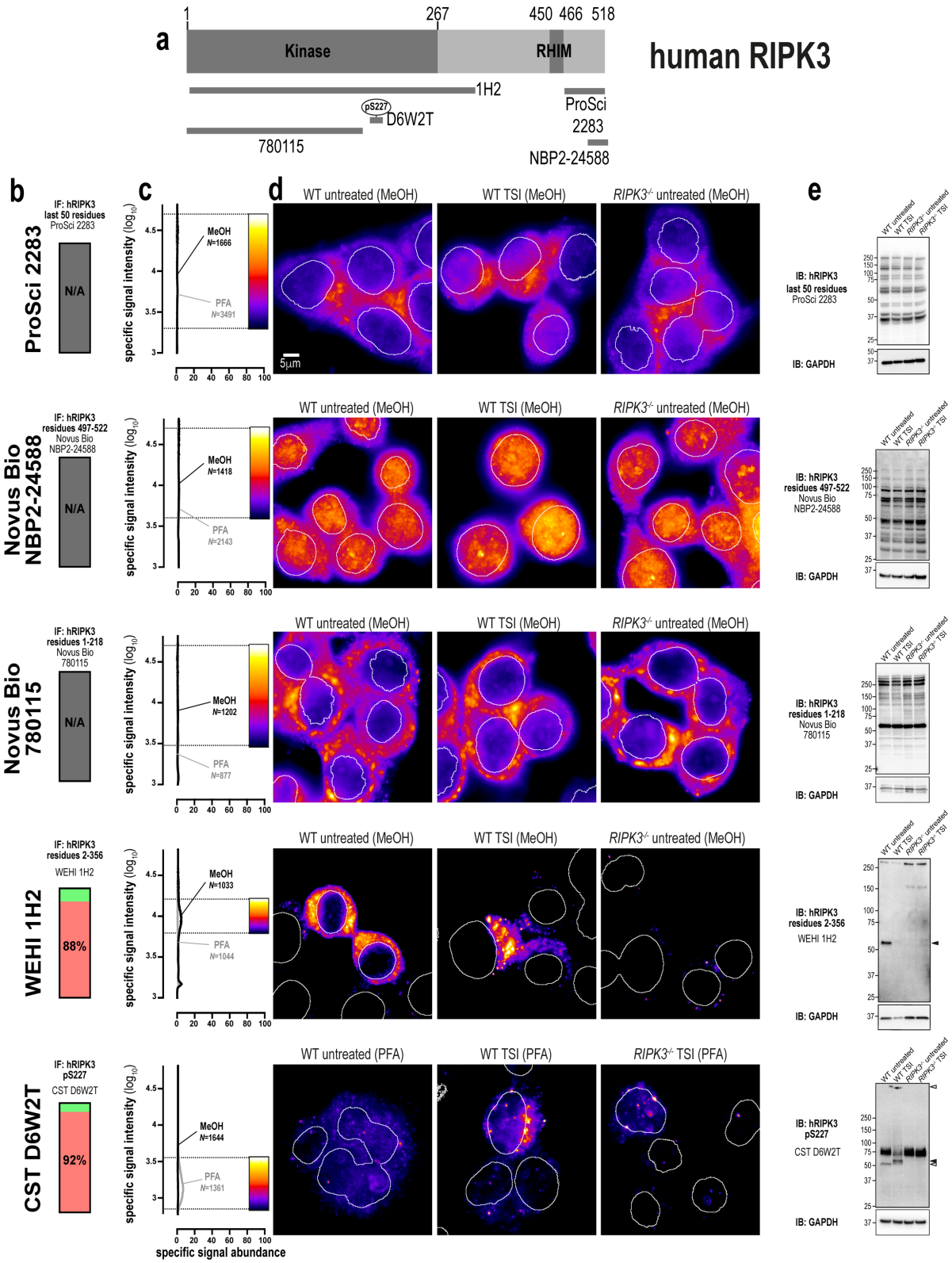

824

825

826 **Figure 2: Better antibodies are needed for imaging human RIPK3.**

827 **a** Human RIPK3 domain architecture showing the immunogens or epitopes for the tested anti-RIPK3
828 antibodies. **b** Quantitation of the percentage of gated signals for the tested RIPK3 antibodies. **c**
829 Quantitation of specific signal abundance produced by the tested RIPK3 antibodies on methanol-
830 fixed (MeOH) or paraformaldehyde-fixed (PFA) HT29 cells. The number of cells imaged (N) to
831 generate each signal-to-noise curve is shown. **d** Micrographs of immunofluorescent signals for the
832 tested RIPK3 antibodies on HT29 cells. As indicated by each pseudocolour look-up-table, only
833 immunosignals within the respective gate in panel **c** were visualised. Data are representative of n=3
834 (Cell Signaling Technology clone D6W2T and in-house clone 1H2) and n=2 (ProSci 2283, Novus
835 Biological NBP2-24588 and MAB7604/clone 780115) independent experiments. Nuclei were
836 detected by Hoechst 33342 staining and are demarked by white outlines in micrographs. **e**
837 Immunoblot using the tested RIPK3 antibodies against wild-type and *RIPK3*$^{-/-}$ HT29 cell lysates.
838 Closed arrowheads indicate the main specific band. Open arrowheads indicate other specific bands
839 of interest. Immunoblots were re-probed for GAPDH as loading control.
840
841

Figure 3

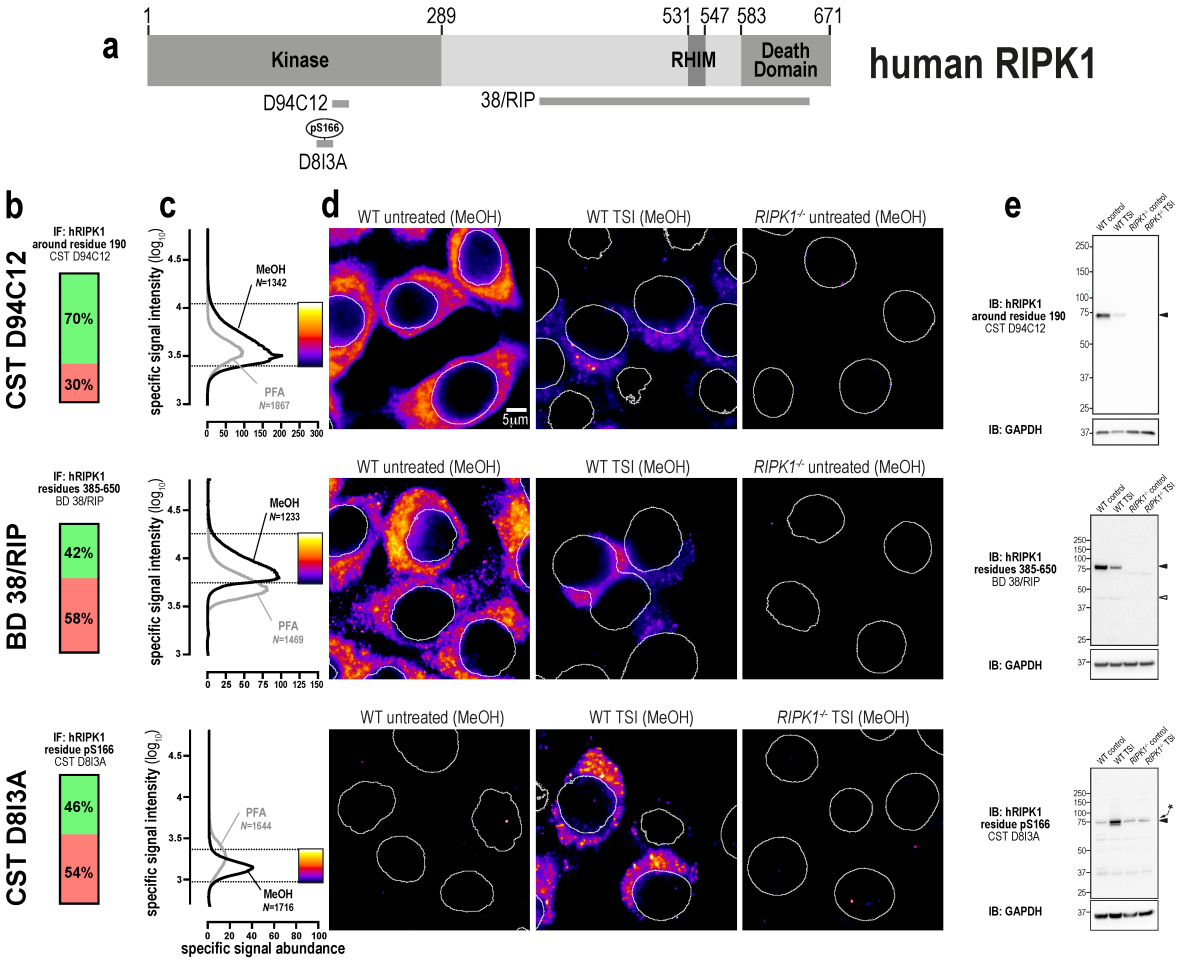

Figure 3: Three specific antibodies for imaging endogenous human RIPK1.

a Human RIPK1 domain architecture showing the immunogens or epitopes for the tested anti-RIPK1 antibodies. **b** Quantitation of the percentage of gated signals for the tested RIPK1 antibodies. **c** Quantitation of specific signal abundance produced by the tested RIPK1 antibodies on methanol-fixed (MeOH) or paraformaldehyde-fixed (PFA) HT29 cells. The number of cells imaged (N) to generate each signal-to-noise curve is shown. **d** Micrographs of immunofluorescent signals for the tested RIPK1 antibodies on HT29 cells. As indicated by each pseudocolour look-up-table, only immunosignals within the respective gate in panel **c** were visualised. Data are representative of n=2 (Cell Signaling Technology clones D94C12 and D8I3A, BD Transduction laboratories clone 38/RIP) independent experiments. Nuclei were detected by Hoechst 33342 staining and are demarked by

853 white outlines in micrographs. **e** Immunoblot using the tested RIPK1 antibodies against wild-type
854 and *RIPK1*$^{-/-}$ HT29 cell lysates. Closed arrowheads indicate the main specific band. Open arrowheads
855 indicate other specific bands of interest. Asterisks indicate non-specific bands that could otherwise
856 confound data interpretation. Immunoblots were re-probed for GAPDH as loading control.
857
858

Figure 4

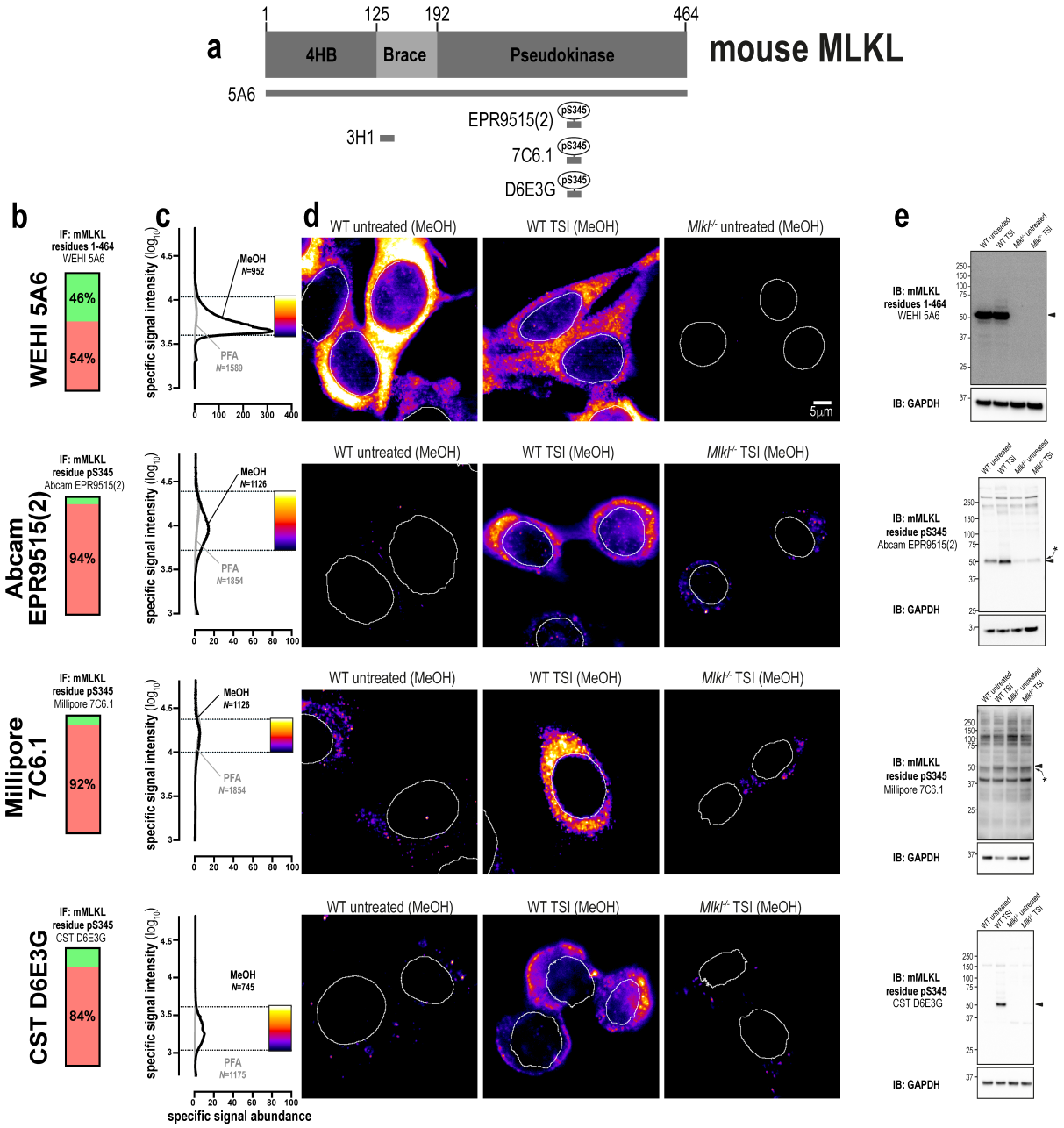

Figure 4: A new monoclonal antibody to image endogenous mouse MLKL.

a Mouse MLKL domain architecture showing the immunogens or epitopes for the tested anti-MLKL antibodies. **b** Quantitation of the percentage of gated signals for the tested MLKL antibodies. **c** Quantitation of specific signal abundance produced by the tested MLKL antibodies on methanol-fixed (MeOH) or paraformaldehyde-fixed (PFA) MDFs. The number of cells imaged (N) to generate each signal-to-noise curve is shown. **d** Micrographs of immunofluorescent signals for the tested

MLKL antibodies on MDFs. As indicated by each pseudocolour look-up-table, only immunosignals within the respective gate in panel **c** were visualised. Data are representative of n=3 (in-house clone 5A6) and n=2 (Abcam clone EPR9515(2), Millipore MABC1158/clone 7C6.1 and Cell Signaling Technology clone D6E3G) independent experiments. Nuclei were detected by Hoechst 33342 staining and are demarked by white outlines in micrographs. **e** Immunoblot using the tested MLKL antibodies against lysates from wild-type and *Mlkl*$^{-/-}$ MDFs. Closed arrowheads indicate the main specific band. Asterisks indicate non-specific bands that could otherwise confound data interpretation. Immunoblots were re-probed for GAPDH as loading control.

Figure 5

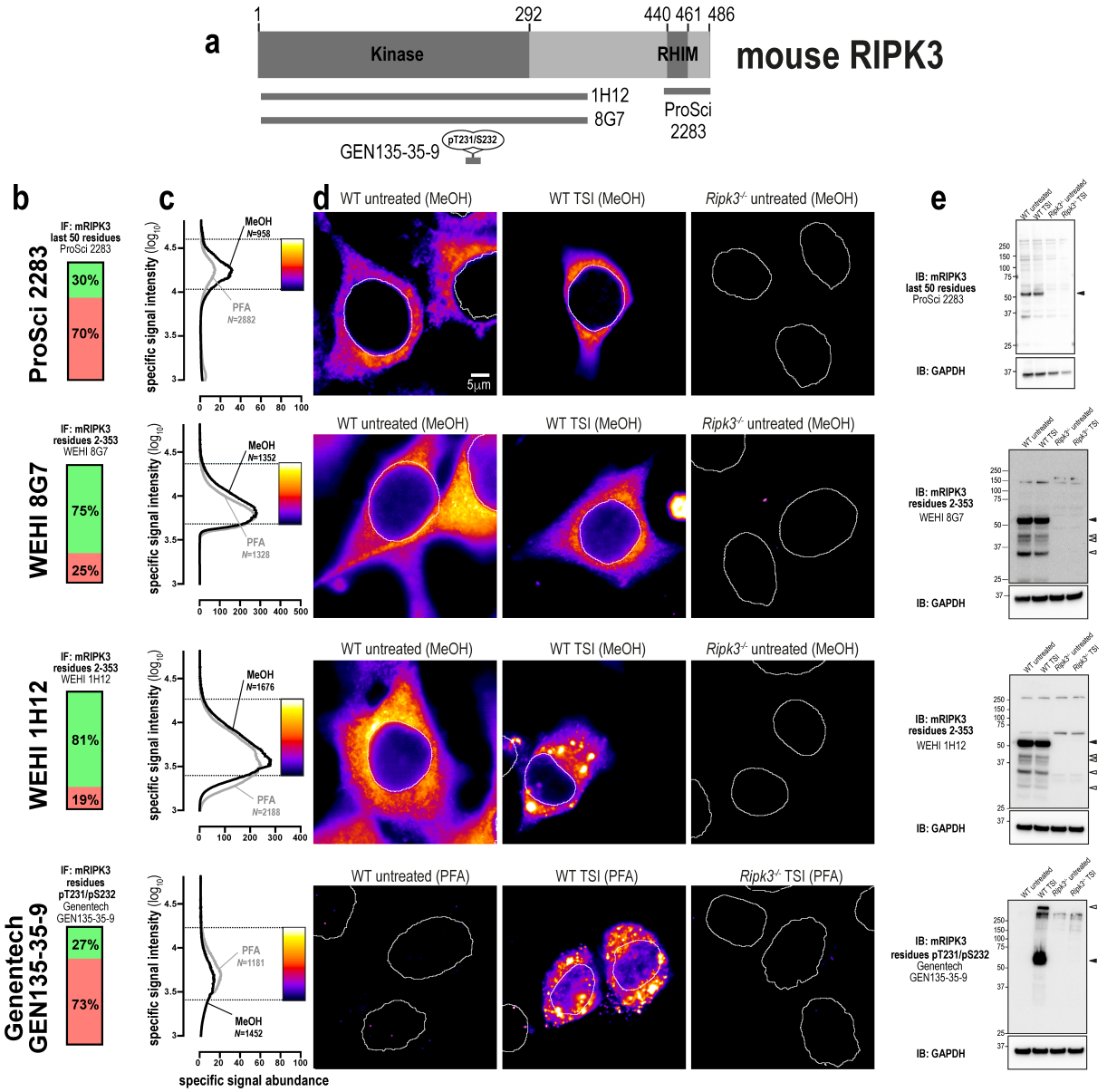

Figure 5: Unlike human RIPK3, mouse RIPK3 is highly amenable to detection by immunofluorescence and immunoblotting.

a Mouse RIPK3 domain architecture showing the immunogens or epitopes for the tested anti-RIPK3 antibodies. **b** Quantitation of the percentage of gated signals for the tested RIPK3 antibodies. **c** Quantitation of specific signal abundance produced by the tested RIPK3 antibodies on methanol-fixed (MeOH) or paraformaldehyde-fixed (PFA) MDFs. The number of cells imaged (N) to generate each signal-to-noise curve is shown. **d** Micrographs of immunofluorescent signals for the tested

884 RIPK3 antibodies on MDFs. As indicated by each pseudocolour look-up-table, only immunosignals
885 within the respective gate in panel **c** were visualised. Data are representative of n=3 (in-house clone
886 8G7 and Genentech clone GEN135-35-9) and n=2 (ProSci 2283, in-house clone 1H12) independent
887 experiments. Nuclei were detected by Hoechst 33342 staining and are demarked by white outlines in
888 micrographs. **e** Immunoblot using the tested RIPK3 antibodies against lysates from wild-type and
889 *Ripk3*$^{-/-}$ MDFs. Closed arrowheads indicate the main specific band. Open arrowheads indicate other
890 specific bands of interest. Immunoblots were re-probed for GAPDH as loading control.
891
892

Figure 6

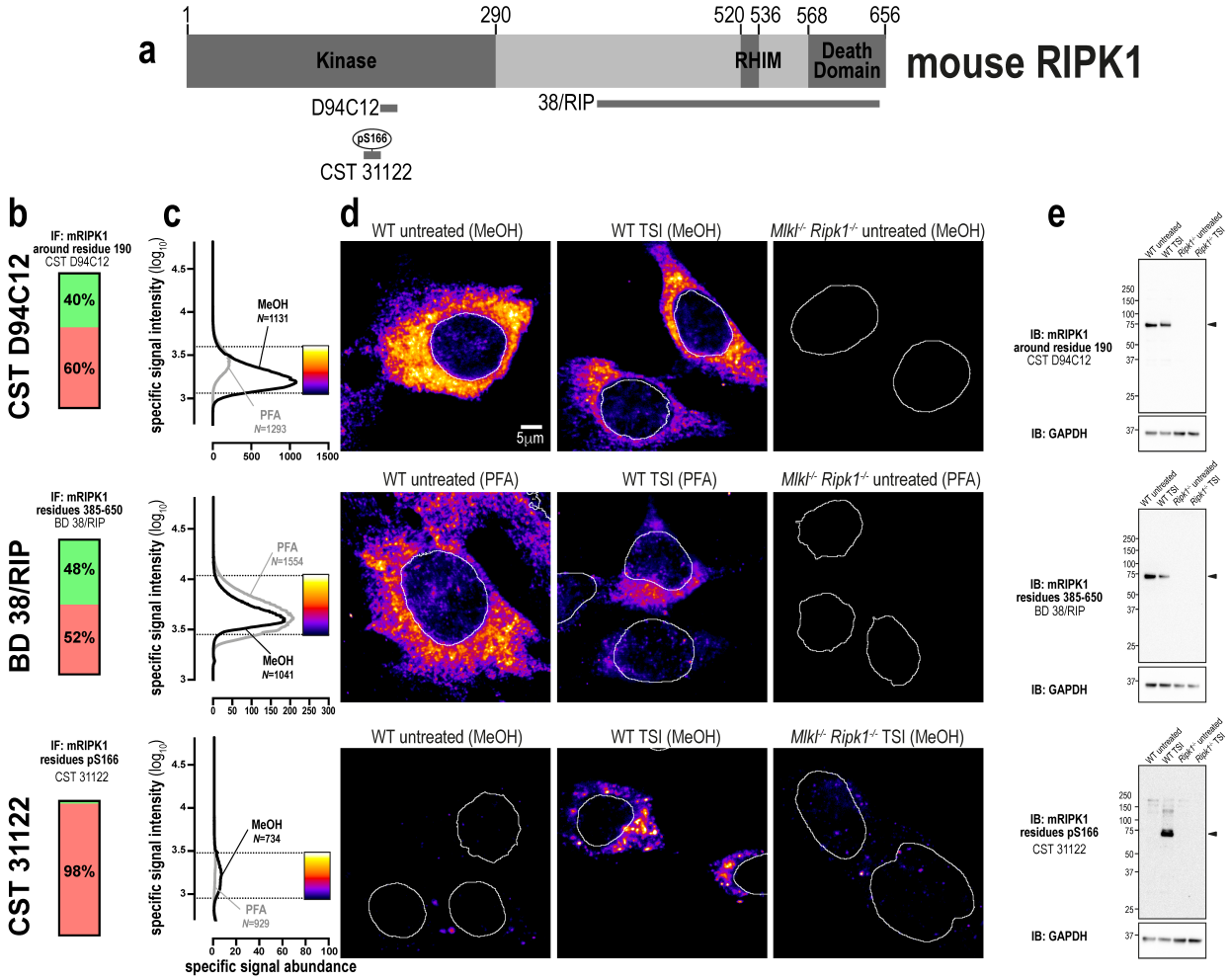

Figure 6: Three specific antibodies for imaging endogenous mouse RIPK1.

a Mouse RIPK1 domain architecture showing the immunogens or epitopes for the tested anti-RIPK1 antibodies. **b** Quantitation of the percentage of gated signals for the tested RIPK1 antibodies. **c** Quantitation of specific signal abundance produced by the tested RIPK1 antibodies on methanol-fixed (MeOH) or paraformaldehyde-fixed (PFA) MDFs. The number of cells imaged (N) to generate each signal-to-noise curve is shown. **d** Micrographs of immunofluorescent signals for the tested RIPK1 antibodies on MDFs. As indicated by each pseudocolour look-up-table, only immunosignals within the respective gate in panel **c** were visualised. Data are representative of n=2 (Cell Signaling Technology clones D94C12 and 31122, and BD Transduction Laboratories clone 38/RIP) independent experiments. Nuclei were detected by Hoechst 33342 staining and are demarked by

904 white outlines in micrographs. **e** Immunoblot using the tested RIPK1 antibodies against lysates from
905 wild-type and *Ripk1*$^{-/-}$ MDFs. Closed arrowheads indicate the main specific band. Open arrowheads
906 indicate other specific bands of interest. Immunoblots were re-probed for GAPDH as loading control.
907
908

Figure 7

a

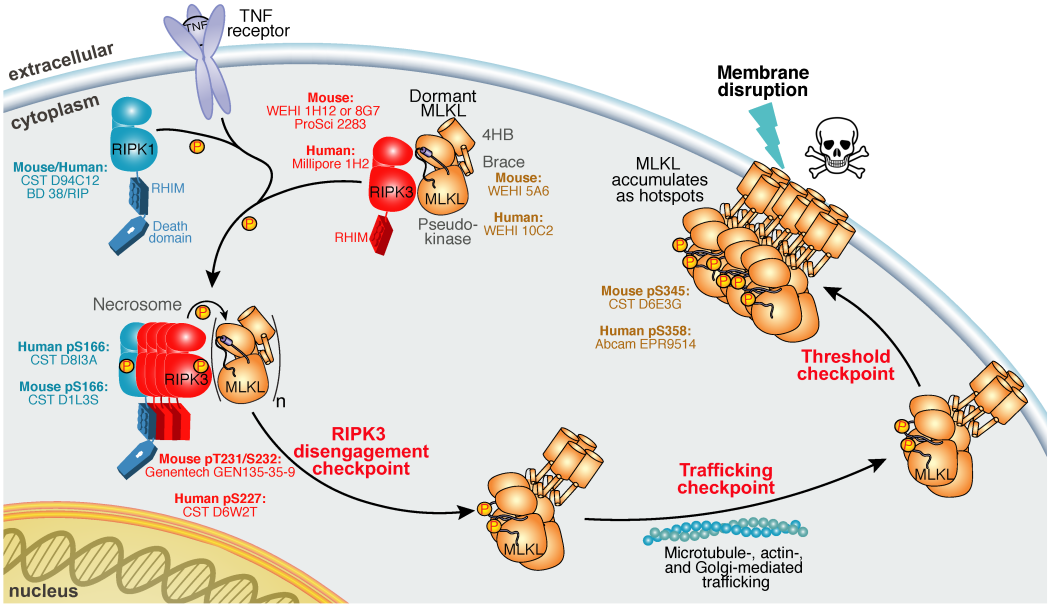

b

	mouse cells			human cells	
	cocktail #1	**cocktail #2**	**cocktail #3**	**cocktail #4**	**cocktail #5**
channel #1 (detected with fluorescent anti-rat IgG)	**MLKL** (clone 5A6) or **RIPK3** (clone 8G7/1H12)	**MLKL** (clone 5A6) or **RIPK3** (clone 8G7/1H12)	**MLKL** (clone 5A6) or **RIPK3** (clone 8G7/1H12)	**MLKL** (clone 10C2) or **RIPK3** (clone 1H2)	**MLKL** (clone 10C2) or **RIPK3** (clone 1H2)
channel #2 (detected with fluorescent anti-rabbit IgG)	**phospho-MLKL** (clone D6E3G)	**phospho-RIPK3** (clone GEN135-35-9)	**phospho-RIPK1** (CST 31122)	**phospho-MLKL** (clone EPR9514)	**phospho-RIPK1** (clone D8I3A)
channel #3 (detected with fluorescent anti-mouse IgG)	**RIPK1** (clone 38/RIP)	**RIPK1** (clone 38/RIP)	**RIPK1** (clone 38/RIP)	**RIPK1** (clone 38/RIP)	**RIPK1** (clone 38/RIP)
channel #4 (suggested counterstains)	**DNA** (Hoechst 33342), **membranes** (biotinylated wheat germ agglutinin added 10 minutes before fixation then detected with fluorescent streptavidin), **microtubules** (anti-tubulin immunofluorescence with Cytoskeleton Inc. # ATN02 then detection with fluorescent anti-sheep IgG), or **early endosomes** (biotinylated transferrin added 10 minutes before fixation then detected with fluorescent streptavidin)				

c

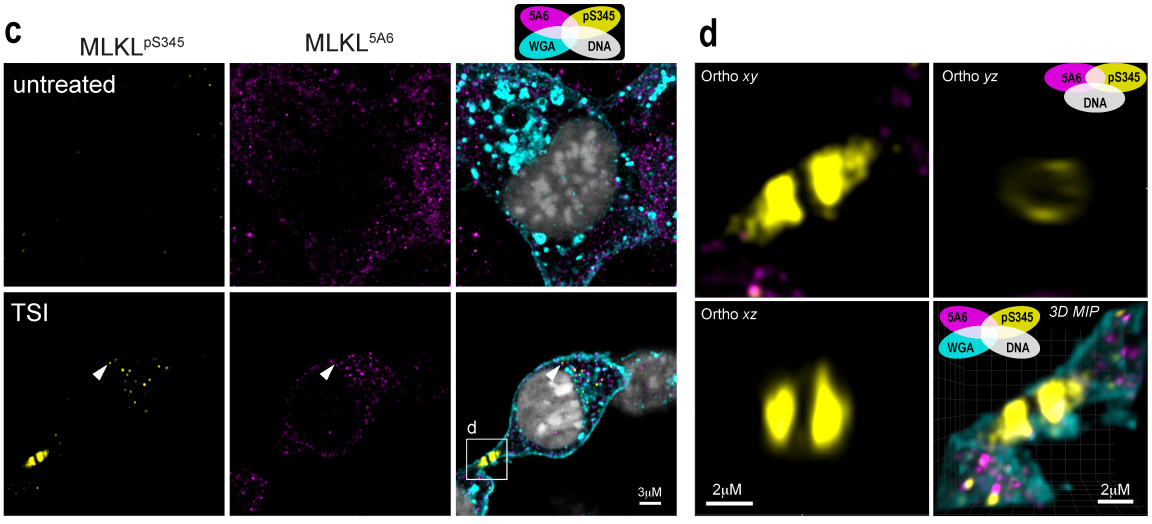

d

Figure 7: Optimised antibody cocktails for visualising endogenous necroptotic signaling in fixed human and mouse cells.

912 **a** Cartoon summary of the currently-understood chronology of TNF-induced necroptosis.
913 Recommendations of validated antibodies for immunostaining various steps in the necroptotic
914 pathway are provided. **b** Summary of validated antibody cocktails and counterstains that can be
915 multiplexed to examine endogenous necroptotic signaling in fixed human and mouse cells. Successful
916 detection of specific signals relies on fixation in methanol, rather than crosslinking fixatives such as
917 paraformaldehyde. **c** Two-dimensional Airyscan micrographs of Wheat Germ Agglutinin (WGA)-
918 stained membranes, Hoechst-stained DNA and anti-MLKL immunosignals from clone 5A6 and clone
919 D6E3G on methanol-fixed wild-type MDFs that had been left untreated or TSI-treated for 60min.
920 Arrowhead exemplifies the small clusters of MLKL that form during necroptosis. The box indicates
921 the junctional accumulation of phospho-MLKL. **d** Three-dimensional orthogonal projections and
922 maximum intensity projection (MIP) of the boxed region from panel **c** showing a ring-like structure
923 adopted by phospho-MLKL at the WGA-stained plasma membrane. Accompanied by Supplementary
924 Video 1.